J Nanostruct 16(1): 1004-1016, Winter 2026

RESEARCH PAPER

A Hybrid Platform Combining Nano Plasmonic U-turn Microfluidics and LIF Detection for High-Throughput Analysis of DNA Damage in Lymphocytes

Rajaa H. Mutlag [1], Zainab AL-Bawi [1], Hazim I. Al-Ahmed [2]*

[1] *Institute of Laser for Postgraduate Studies, University of Baghdad, Iraq*

[2] *Biotechnology Research Center, University of Al-Nahrain, Baghdad, Iraq*

ARTICLE INFO

Article History:
Received 03 September 2025
Accepted 24 December 2025
Published 01 January 2026

Keywords:
Early Cancer Detection
DNA Fragmentation
Optofluidic Biosensor
Plasmonic Enhancement
Point-of-Care Diagnostics

ABSTRACT

A microchip-based spiral system was fabricated with an integrated laser-induced fluorescence setup to study the size of genetic material preceding cancer onset. The chip was designed with three inlets: one for the isolated genetic material, the second for acridine orange dye, and the third for rhodamine dye at four different concentrations to determine the optimal energy transfer efficiency. In healthy cells, a single distinct emission peak appeared around 520 nm, while an additional peak extended toward 590 nm, alongside the green emission. The ratio of these peaks varied with the degree of structural degradation. When mixed with rhodamine, the 1:1.5 ratio produced the best energy transfer before photobleaching occurred. The gold coating, leveraging a plasmonic effect, and a smooth laminar flow significantly boost the signal clarity and minimized the need for reagents. This work represents a parallel step toward early cancer detection when conventional methods fail, reducing both the physical and psychological burden experienced by patients during routine examinations.

How to cite this article
Mutlag R., AL-Bawi Z., Al-Ahmed H. A Hybrid Platform Combining Nano Plasmonic U-turn Microfluidics and LIF Detection for High-Throughput Analysis of DNA Damage in Lymphocytes. J Nanostruct, 2026; 16(1):1004-1016. DOI: 10.22052/JNS.2026.01.090

INTRODUCTION

Damage to DNA can change nucleotide sequences and cause malfunctioning proteins to be expressed, which can affect normal cellular physiology, And through Cancer treatments (especially chemotherapy and radiotherapy) can adversely effect on hematology order [1,2]. Since greater fragmentation causes genomic instability, which makes it easier for mutations to accumulate and malignant transformation to occur, DNA fragmentation is thought to be one of the processes linked to the development of cancer. Research has demonstrated that poor DNA fragmentation repair raises the risk of cancer, especially in tumors that have mutations in repair genes like BRCA1/2. Furthermore, quantifying DNA fragment byproducts be a useful diagnostic indicator for the early identification of specific malignancies [3-5]. Radiation exposure, chemotherapeutic drugs, oxidative stress, and apoptotic processes can all cause DNA fragmentation [6]. It includes double-strand breaks (DSBs) from ionizing radiation and single-strand breaks (SSBs) from metabolic byproducts [7]. Pathological fragmentation is caused by replication mistakes, whereas programmed fragmentation occurs during

* *Corresponding Author Email: rajaie.hamil2101p@ilps.uobaghdad.edu.iq*

apoptosis, because persistent DSBs we have the potential to cause chromosomal translocations [8].

Among versatile fluorescent dye, Acridine Orange (AO) exhibits differential binding to nucleic acids, producing red fluorescence when complexed with single-stranded nucleic acids (RNA or denatured DNA) and green fluorescence when intercalated with double-stranded DNA [9]. Since apoptotic cells show higher red fluorescence because of increased RNA accessibility and DNA breakage. This characteristic makes it very useful for cell cycle analysis and apoptosis detection, allowing for the early detection of nuclear changes [10]. AO enables the detection of nuclear morphological changes during programmed cell death when paired with fluorescence microscopy for three reasons [11]:

1. Nucleic Acid Binding Specificity: Because of differential stacking interactions, AO shows a green-to-red fluorescence shift when binding to dsDNA (λem=530 nm) as opposed to ssRNA/ denatured DNA (λem=640 nm) [12].

2. Status of Cellular Viability: Increased red fluorescence is seen in apoptotic cells from(a) RNA exposure during membrane degradation (b)DNA denaturation in fragmented nuclei [13].

3. pH-Dependent Aggregation: In acidic compartments (lysosomes), AO dimers or aggregates produce red spectral shifts that are helpful for autophagy research [14].

Because Acridine Orange (AO) can cause mutagenesis by interfering with DNA replication, it may be lethal at high quantities [15].

Modern laboratories have undergone a revolution because of microfluidic chips, which allow for precise fluid manipulation at the microscale, greatly lowering sample and reagent usage while improving analytical performance [16]. These miniature devices provide quick, high-throughput, and reasonably priced solutions for chemical and biological studies by combining several laboratory tasks like mixing, separation, and detection into a single chip [17, 18]. Utilizing laminar flow and diffusion-dominated phenomena specific to microscale fluid dynamics, their applications extend to point-of-care testing, drug development, and diagnostics. Microfluidic technology is a flexible platform that keeps advancing lab-on-a-chip and personalized medicine [19, 20].

Lab-on-paper is a low-cost, portable, and user-friendly alternative manufacturing method that has a lot of promise for mechanisms for food safety, environmentally friendly protection, and forensic science [21]. Because of its high sensitivity, specificity, and real-time monitoring capabilities, fluorescence detection is an essential analytical technique that is used in DNA sequencing, cellular imaging, and biomedical diagnostics [22]. In certain applications, single-molecule detection is made possible by its high signal-to-noise ratios and low background noise, which contribute to its accuracy [23], Researchers have developed numerous sensors using various optical techniques. Key platforms among these are Surface-Enhanced Raman Spectroscopy (SERS) [24], Mach-Zehnder Interferometers (MZI) both single and cascaded [25,26]. Multi-Mode Interference (MMI) devices [27], and fiber-optic sensors built with coreless fiber and an offset coreless fiber design [28, 29].

Many biosensors Plasmonic nanostructures, such as gold nanoparticles, are used to further improve fluorescence signals by using surface plasmon resonance (SPR) to increase emission intensity through localized electric field enhancement [30] by optimizing light-matter interactions, methods like plasmonic nanoantenna design and metal-enhanced fluorescence (MEF) greatly increase detection limits [31].

In Fluorescence Resonance Energy Transfer (FRET), energy is transferred non-radiatively from an excited donor fluorophore to an acceptor chromophore through long-range dipole-dipole coupling [32] for reviews see [33, 34]. A novel method for assessing DNA fragmentation in lymphocytes is presented, employing a gold-coated microchannel platform. The sensitivity is significantly amplified by coupling laser-induced fluorescence detection with the signal enhancement mechanisms of localized plasmon resonance and FRET.

MATERIALS AND METHODS

Ethical Approval and Lymphocyte Isolation

Peripheral blood samples were collected from two groups:12 healthy female donors (22-25 years) and 15 women newly diagnosed breast cancer with invasive Ductal Carcinoma (IDC), low grade, with Ductal Carcinoma in Situ (DCIS) involved margin. following informed consent and ethical approval from the relevant situational review board. Each subject provided 5 mL of venous

blood collected in EDTA-treated tubes. To isolate lymphocytes, 3 mL of phosphate-buffered saline (PBS) was added to each blood sample to maintain isotonic conditions, followed by density gradient centrifugation using Ficoll-Paque. The mixture was centrifuged at 400 × g for 30–45 minutes, yielding distinct layers, including a buffy coat containing mononuclear cells, see Fig. 1.

The lymphocyte layer was carefully extracted, washed repeatedly with PBS to remove residual platelets and Ficoll, and suspended in RPMI-1640 medium supplemented with 9% fetal bovine serum and L-glutamine. The cells were incubated at 37 °C with 5% CO_2 and 95% relative humidity for 24 hours to ensure viability prior to staining.

Microfluidic Chip Fabrication and Configuration

Microfluidic channels were fabricated on highly transparent poly(methyl methacrylate) (PMMA) sheets with a thickness of 2.5 mm (supplied by Jumei Acrylic Manufacturing, Shanghai, China). The engraving process was performed using a high-power CO2 laser system (Liaocheng JK-4060, China) operating at an output power of 60 W. The laser beam was focused to a spot diameter of approximately 55 µm. The laser head, equipped with a focal lens and mounted on a three-axis (x, y, z) translation stage, was traversed at a constant scan speed of 250 mm/s to engrave the desired micro-line patterns. Prior to machining, the protective coating was removed from the PMMA sheets to prevent interference with the engraving process. The integrated laser system included auxiliary components for process control, namely an air compressor, a cooling unit, and an exhaust system.(see Fig. 2)

Microchannels offer the advantage of an increased surface area to volume ratio in many biological applications, which reduces reagent and sample consumption while enhancing the reaction of surfaces [35]. A critical component of microfluidic devices is the micromixer chip designed to provide excellent mixing of two or more incoming microfluidic streams. Understanding the stream dynamics within a microfluidic chip, we recognize two types of fluid flow:

1. laminar flow: characterized by a parabolic velocity profile, where the flow speed is greatest at the centerline of the channel.

2. Turbulent flow: at this pattern, molecules move in irregular directions due to Flow eddies, this movement can be characterized by oscillations, contrasting with the orderly motion seen in laminar flow.

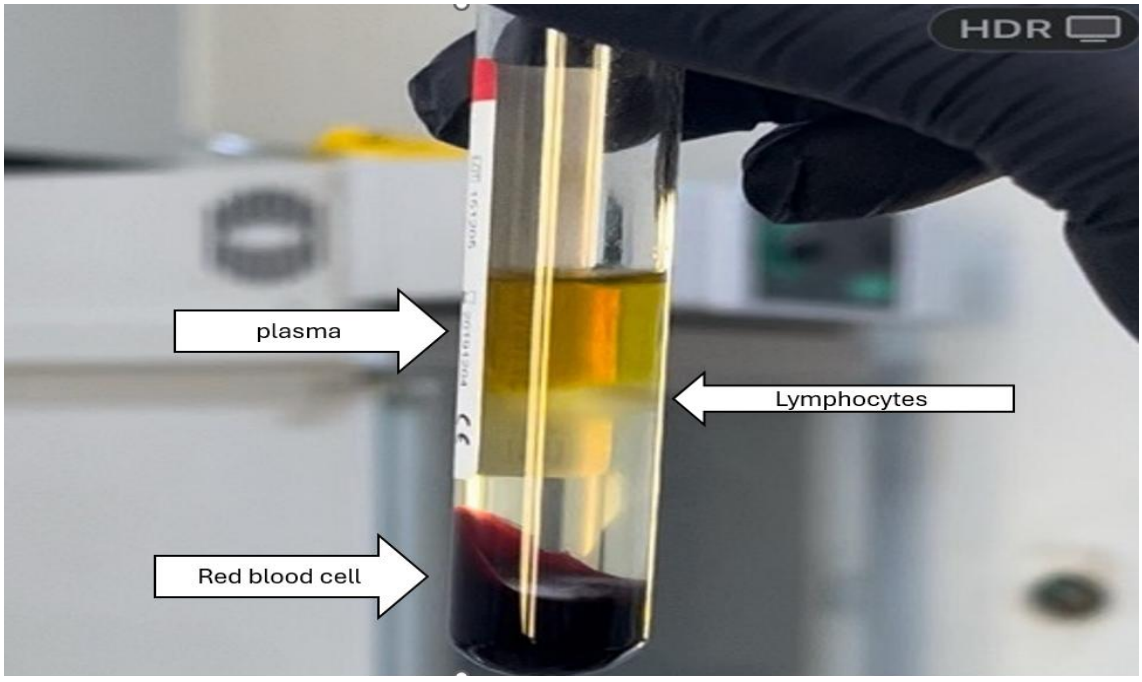

Fig. 1. Blood separation with Ficoll gradients.

The kinematic viscosity (Table1) is measured using an UBBELOHDE VISCOSIMETER at a temperature of 40°C for 3 seconds in the Department of Oil and Petro Research, Scientific Research Commission, Baghdad, Iraq. Additionally, the density of liquids is determined at 20°C using a condenser in the Department of Advanced Material Research, Scientific Research Commission, Baghdad, Iraq. As shown, intact DNA has Higher viscosity due to entangled DNA chains increase resistance to flow (higher intrinsic viscosity).

Among the advantages of mixing (or staining) under laminar flow are high homogeneity without bubbles, precise control over flow rate and pressure using micro-pumps, and the absence of mechanical stress on cells or proteins. However, despite these tremendous benefits, there are still challenges related to manufacturing costs and design complexity. Nevertheless, the future direction is clearly moving toward producing low-cost devices to make precision medicine accessible to everyone.

The sputter coating process, which involves applying a thin layer of gold (see Fig. 3) onto a PMMA substrate. Produces channels that are significantly smoother than their untreated counterparts. This improvement in microchannel surface quality is crucial for the optimal performance of microfluidic devices. By increasing the contact area between the sample and the metal film, we enhance energy coupling between the plasmon mode and the fluid, making it more efficient. It is imperative to thoroughly investigate the effects of surface roughness on fluid flow in microchannels. Process parameters such as injection speed and laser power can lead to the formation of solidified particles, drastically increasing surface roughness. Addressing these issues is essential for advancing microfluidic technology.

Energy Dispersive X-ray (EDX) elemental analysis was performed on the polymer samples. Chloroform was used as an intermediate layer to create PMMA-PMMA structures. Since chloroform Since adhesives are believed to be biocompatible, direct contact with the components inside the

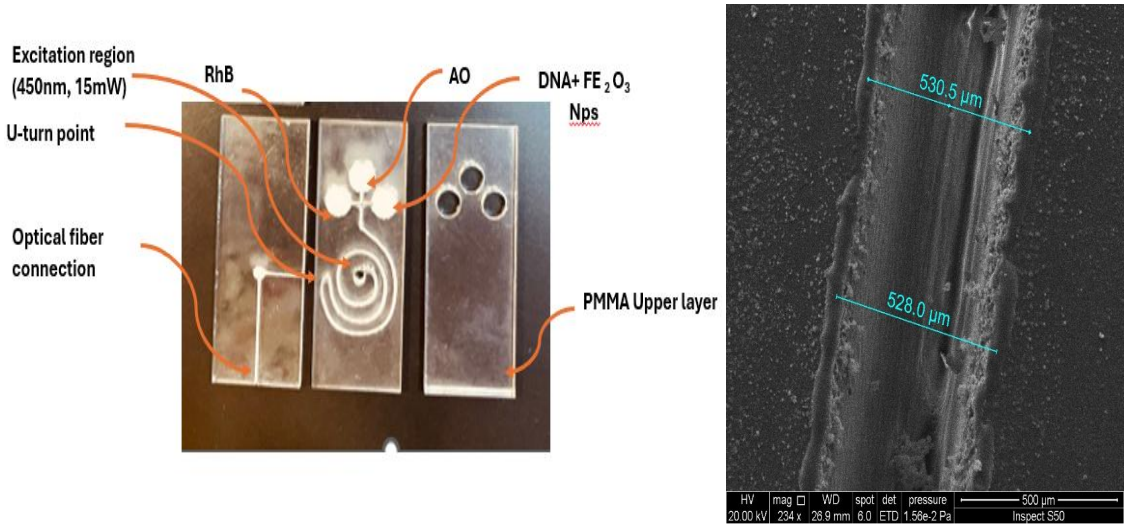

Fig. 2. PMMA spiral -U micro mixer (left) channel width (right).

Table 1. Flow rate at micromixer (channel width 446 µm, Hight: 144µm, length 28mm).

Sample	Pressure (mBar)	Re	Fluid viscosity (pa.s)	Density kg/cm^3	Flow rate (µL/min)
Intact DNA + AO	0.01	4.84e-3	0.00156	0.992	0.16
Fragmented DNA+ AO	0.01	5.01 e-3	0.001528	1.006	0.16

microchannels is not a concern. Fig. 3 shows peaks from the gold (EDX) spectra for the PMMA and adhesive chloroform elemental compositions. The findings supported PMMA's acrylic-rich nature, and revealed that it was primarily made of carbon (C) and oxygen (O). The presence of these substances will produce charges on the polymer's surface and electrostatic forces that will draw the sample and chloroform solution together. Electrostatic contact can cause the chloroform solution to adhere to PMMA surfaces, in agreement with [36, 37].

As a result of its low surface energy (41.1 mN m-1), PMMA is very wettable. Substrates with more surface energy or wettability have a higher bonding propensity. Water contact angles for surfaces before and after coating were measured, and it was discovered that the latter had a larger angle than the former. This finding suggests that coating increased the substrates' surface energy, enhancing the surfaces' wettability or hydrophilicity. Fig. 4 shows the contact angle values for microfluidic devices the PMMA contact angle values (40.37° and 73.57°, respectively) before and after coating. The hydrophilic PMMA surface's contact angle increased as the roughness gradually decreased, so the flow rate increased when the roughness decreased, were in good agreement with published studies [38, 39].

A blue laser (15 mW) beam is totally internally reflected at the interface between a solid substrate (PMMA) and the liquid droplet. This internal reflection generates an *evanescent electromagnetic field* that penetrates the liquid phase, but only for a very short distance (typically

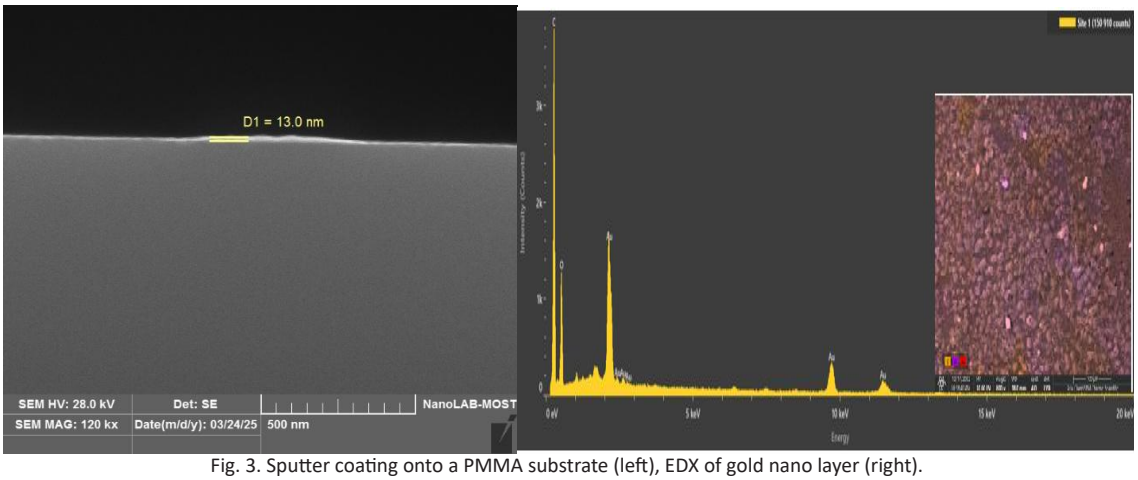

Fig. 3. Sputter coating onto a PMMA substrate (left), EDX of gold nano layer (right).

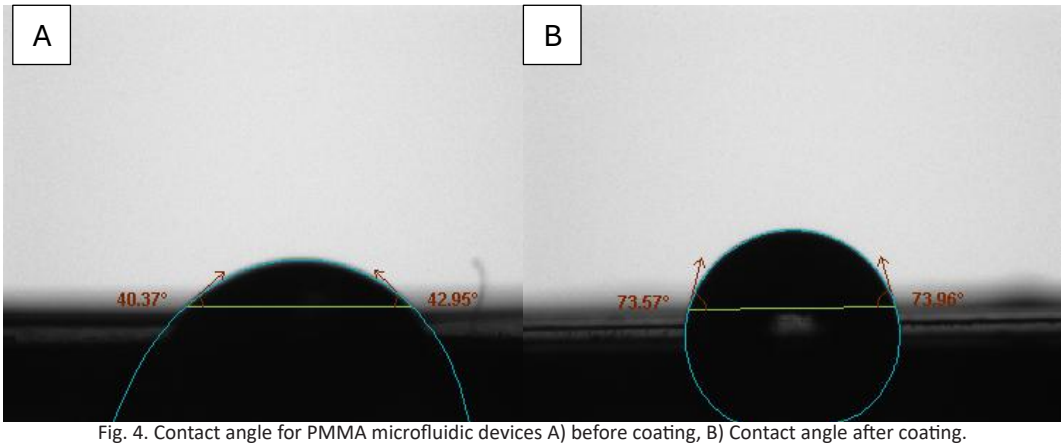

Fig. 4. Contact angle for PMMA microfluidic devices A) before coating, B) Contact angle after coating.

~100-200 nm). This evanescent field selectively excites fluorescent molecules that are very close to the solid-liquid interface, as a Result we get a dramatically enhanced signal-to-noise ratio for events happening specifically at the interface of interest, right where the contact angle is defined [40-43].

Optical and structural characterization of material

Acridine Derivatives: Exhibit distinct FTIR peaks for amine, carbonyl, and aromatic vibrations as shown in Fig. 5 Strong absorption of about 1693 cm^{-1} Carbonyl (C=O) due to dye binding and broad Hydroxyl (O-H) 3435 cm^{-1} from polysaccharides, and Amine (N-H) 1540 cm^{-1} involvement in biosorption. that's agree with [44, 45].

Structural Fingerprints for RhB is aromatic (1500–1600 cm^{-1}) The broad signal centered around 3400 cm^{-1} can be attributed to O-H stretching vibrations including that of adsorbed water molecules. The peak at 1575 cm^{-1} can be assigned to symmetric stretching vibrations of C=C bonds. That's with [46].

Hematite's crystal structure (hexagonal) leads to distinct Fe-O vibrations in the far-IR region, therefore Strong, broad peak antisymmetric Fe-O stretching in octahedral sites extend from 540–580 cm^{-1} and 3400 cm^{-1} Broad band appear due to adsorbed water or surface - groups that's with [47, 48].

The plasmon phenomenon often evokes thoughts of the visible spectrum region, but when analyzing FTIR spectra of multiple materials observed similarities in certain peaks may arise due to fundamental structural overlaps or require deeper analytical interpretation. For example, C=O in Rh B ~1670 cm^{-1} and O ~1650 cm^{-1}.

So, the selection of dyes and nanomaterials to correspond with the absorption peaks was effective.

Dispersions of 0.001 g /L Hematite (α-Fe_2O_3) nanoparticles in DIW were prepared and sonicated for 10 min and stirred further 1 h. The isolated cell environment and the nanomaterial solution were forced through saying pump to get plasmonic effect (first aim) and to get anti-bacterial environment. Fig. 6 shows that virgin particles have a rough spherical structure. Indicating the aggregation of particles with small grains present at a surface.

RESULTS AND DISCUSSION

Absorption spectrum by An SP 3000 spectrometer, featuring a 10 W tungsten halogen lamp, was employed to capture the absorbance spectrum using a standard quartz cell to analyze liquids across a wavelength range of 190 nm to 1100 nm, with a silicon photodiode detector. The results revealed striking absorption peaks at 277 nm and 279 nm for both unstained healthy cells and fragmented cells, indicating the presence of

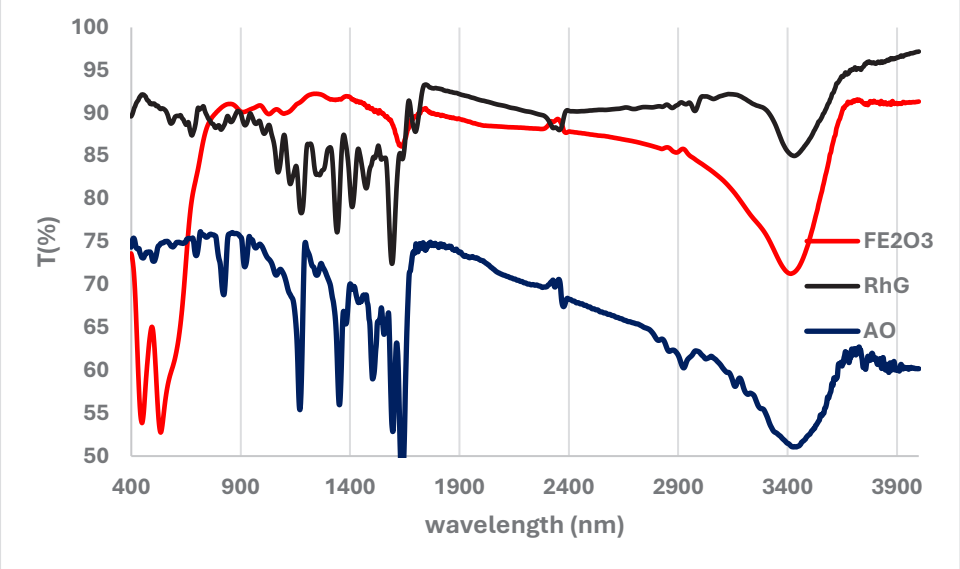

Fig. 5. FTIR for AO, RhB and FE_2O_3NPs.

highly concentrated proteins (see Fig. 7). Notably, healthy lymphocytes generally have lower RNA levels compared to rapidly proliferating cancer cells, which showed no significant variation in the UV range. This finding suggests that the patient may have been newly diagnosed, consistent with the observations made by Thais P. Pivetta et al. [49].

Under identical conditions after staining with acridine dye, variations in cell membrane permeability can significantly influence the amount of dye uptake; thus, cancer cells tend to absorb more dye, resulting in a shift towards a longer wavelength that correlates with RNA levels. Specifically, 492 nm represents the maximum absorbance for healthy cells, while 494 nm corresponds to fragmented stained cells. During staining with Acridine Orange (AO), it does not alter the chemical structure of the genetic material. Instead, it acts as an intercalating agent that interacts with it through the mechanism of intercalation between the base pairs of double-stranded nucleic acids, or via ionic binding (electrostatic attraction) to the phosphate groups of the sugar-phosphate backbone in denatured or single-stranded regions.

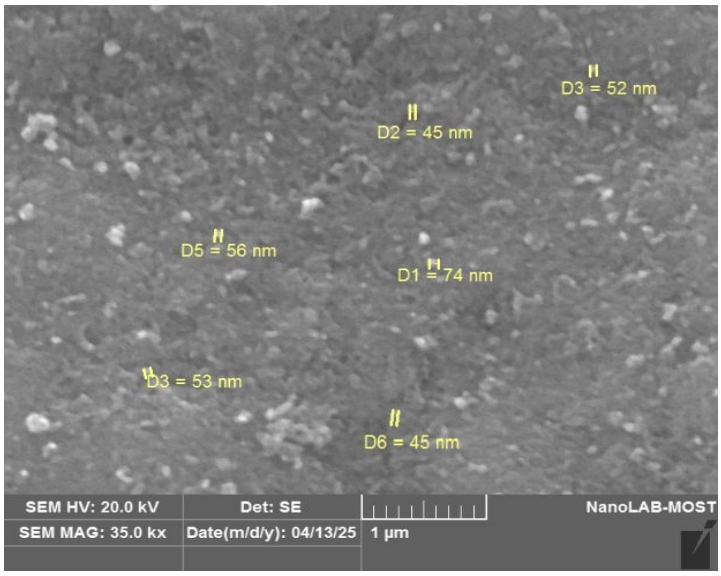

Fig. 6. SEM for α-Fe_2O_3 nanoparticles.

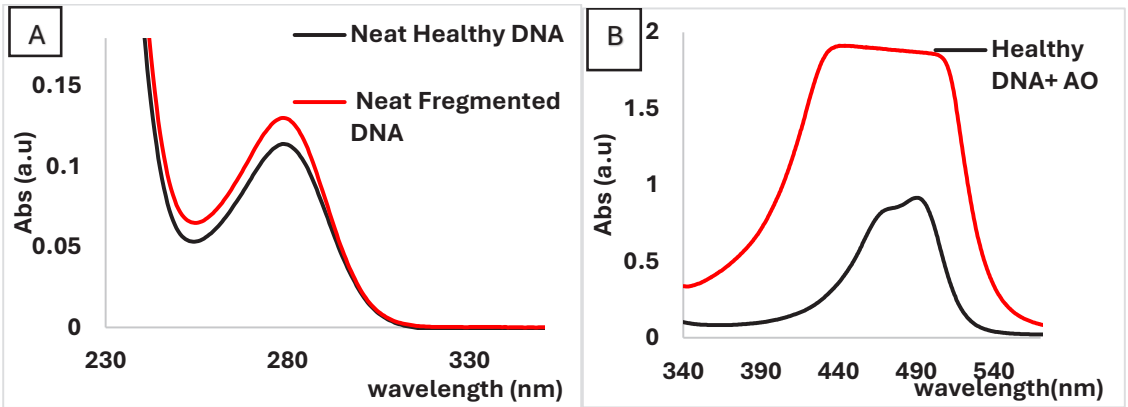

Fig. 7. Absorption spectrum A) without staining B) stained with AO.

The figure below shows the absorption of AO dye at a concentration like that used in fluorescent microscopy staining ($5*10^{-6}$M), as well as three different concentrations of RhB dye with ratios (1:1), (1:1.5), and (1:2). At first glance, the following can be observed:

I. Acridine dyes have a primary absorption peak in the blue light region (typically around 460 nm), while Rhodamine dyes absorb at longer wavelengths (peaks at ~541 nm). This means that Acridine efficiently absorbs blue light, while Rhodamine efficiently absorbs green light.

II. The absorption of light in these dyes is linked to the presence of chromophores in their molecular structure. The molecules of both Acridine and Rhodamine contain conjugated aromatic rings that absorb light in the ultraviolet and visible regions of the spectrum. Dyes with a more extensive conjugated system tend to absorb light at longer wavelengths.

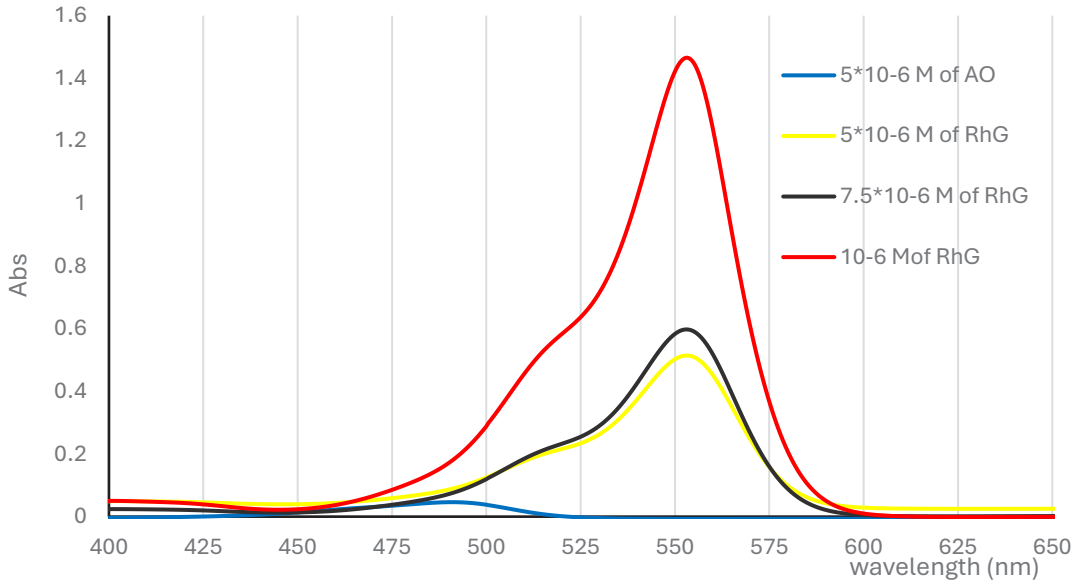

Fig. 8. absorption spectrum for AO and three concentrations of RhG.

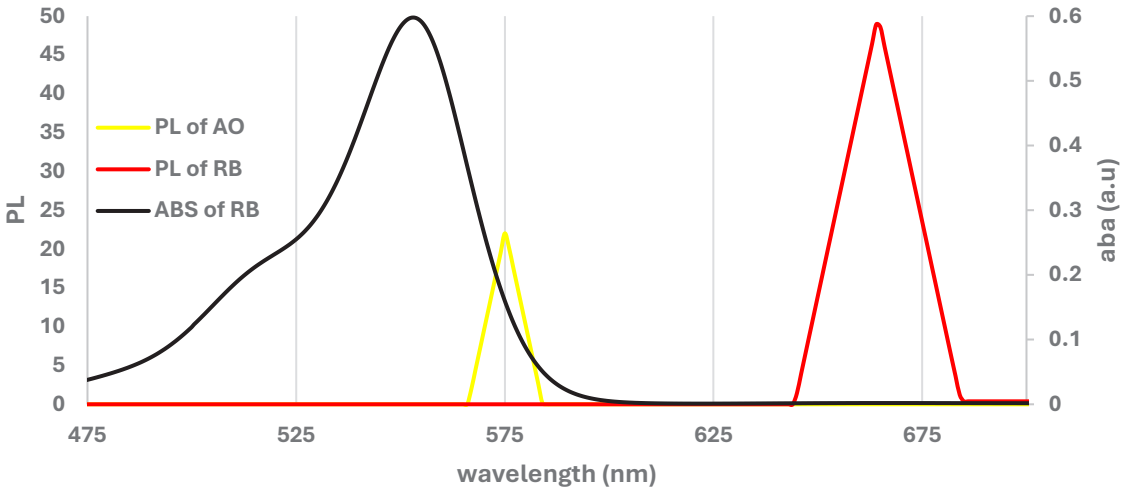

Fig. 9. PL and ABS for AC and RhG.

III. Neither standard Acridine nor Rhodamine dyes have significant absorption in the far-red region (>600 nm). However, advanced rhodamine derivatives (like Texas Red) are engineered to absorb and emit in the red spectrum, that's with [50].

IV. Ao requires a blue light source (laser diode) for optimal excitation, whereas Rhodamine is best excited by green or yellow light (fluorescence of AO), The clear separation between their absorption spectra allows them to be used together in multiplex assays (e.g., imaging two different cellular targets simultaneously) with minimal spectral overlap.

Fig. 9 shows the PL for both AO (donor) and RhG (accepter) When acridine (donor) emits light that overlaps with rhodamine's (acceptor) absorption, energy transfers via FRET, enhancing rhodamine's fluorescence at red-shifted wavelengths. This occurs due to efficient non-radiative dipole coupling, quenching acridine's emission while amplifying rhodamine's signal. The process is distance-dependent (1–10 nm) and useful in sensors and imaging.

LIF spectrum

Laser-Induced Fluorescence (LIF) achieves one of the lowest detections limits due to the coherence

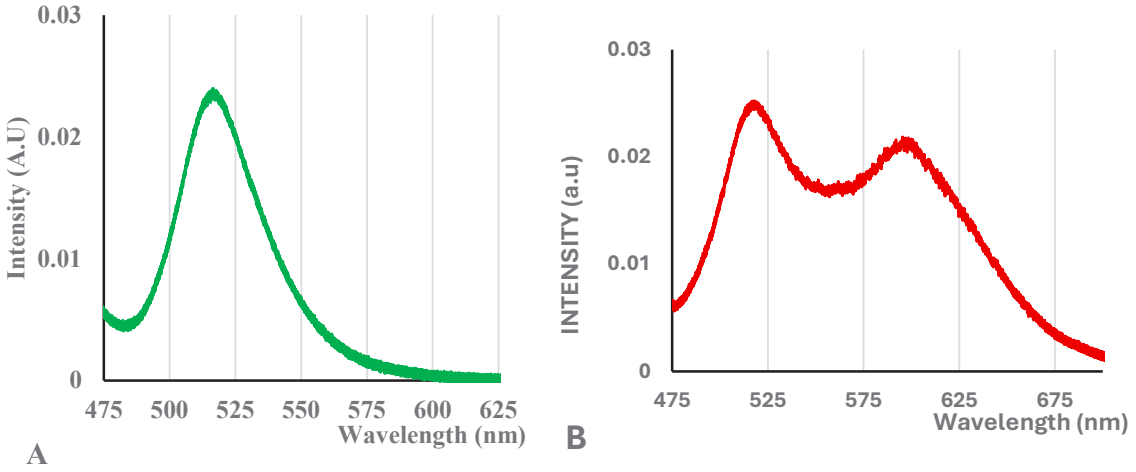

Fig. 10. LIF by blue laser with 15mw for A) intact DNA B) fragmented DNA.

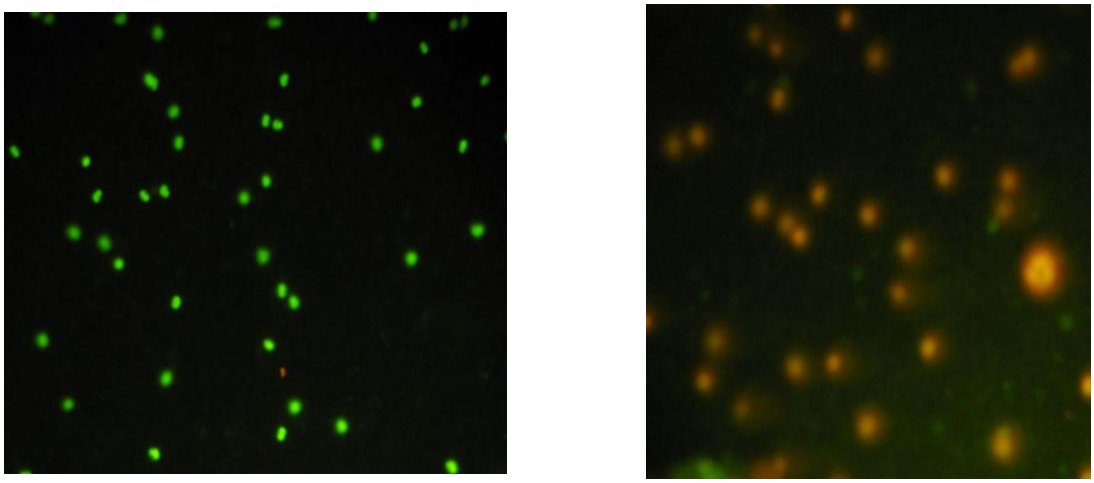

Fig. 11. Florescence microscope image for intact DNA (left) fragmented DNA (right).

and low divergence of lasers, allowing for precise focusing on very small detection volumes and delivering exceptionally high irradiation. With a 90-degree excitation, dye molecules effectively absorb photons, transitioning from the ground state (s0) to an excited singlet state (s1). Then, they undergo vibrational relaxation to the lowest level of s1 before returning to s0 and emitting fluorescence light, Fig. 10 illustrates the fluorescence induced by blue excitation at 15 mW. This evidence unequivocally highlights the critical differences in cellular composition between healthy and cancerous cells, emphasizing the imperative nature of early diagnosis in cancer detection.

The green fluorescence appears because Acridine Orange intercalates between the base pairs of intact, double-stranded DNA. This intercalation locks the dye in a stable, hydrophobic, and planar environment created by the stacked bases, which promotes green emission. When DNA becomes denatured or single-stranded, Acridine Orange binds electrostatically instead, altering its environment and shifting fluorescence toward red or orange [51].

Fluorescence resonance energy transfer between acridine orange and rhodamine B

Fig. 12 shows the fluorescence induced energy transfer; intensity of Rhodamine is higher and more efficient. It is more resistant to photobleaching, more stable in long-term applications, and less affected by environmental conditions. Moreover, the emission intensity of Rhodamine extends into the pink/red region as it receives energy transferred from Acridine Orange. By applying three concentrations of RhG.

From the figure above we can note:

DNA+AOonly

When AO intercalates between the base pairs of double-stranded DNA (dsDNA), its quantum yield and excited-state lifetime rise, producing a strong green emission around ~520 nm. The smaller red shoulder near 590 nm reflects “metachromasy”: AO bound to single-stranded or disordered DNA regions, or aggregated AO molecules. This shift toward red is a classic AO signature—green for

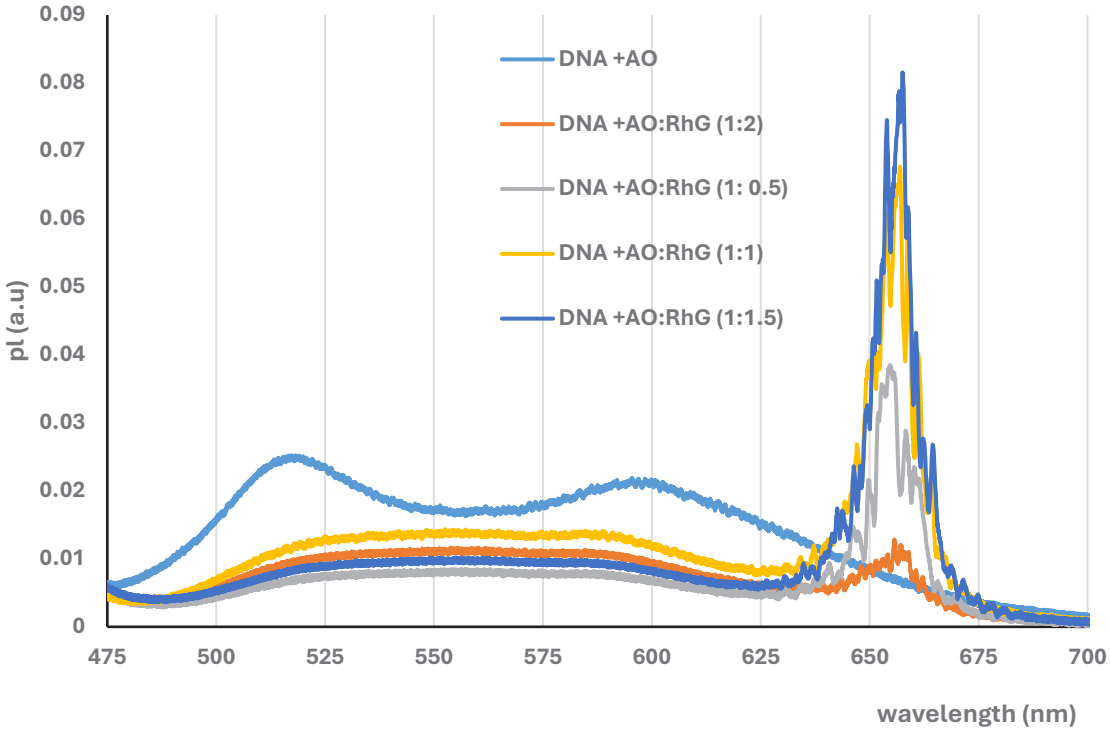

Fig. 12. Fluorescence spectra using 454nm laser (15mW) as the excitation source for newly diagnosed B.C.

Table 2. Quantify energy-transfer efficiency.

AO: RhG ratio	F_D/F_{DA}	Transfer efficiency
1:0.5	0.0085/0.024	≈64.6%
1:1	0.0120/0.024	≈50.0%
1:1.5	0.0070/0.024	≈ 70.8%
1:2	0.0105/0.024	≈56.3%

dsDNA, red for ssDNA or aggregated AO.

DNA+AO:RhB mixtures

Adding RhB reduces the green AO band because AO emission overlaps strongly with the absorption of Rh6G (440–570 nm, max ≈ 530 nm). This overlap enables *Förster resonance energy transfer* (FRET): AO acts as donor, RhB as acceptor. The result AO's green light is quenched. However, your dominant peak lies near 650 nm, not 560 nm (the usual Rh6G emission). This implies that red emission mainly comes from AO's aggregated "metachromatic" state, which RhB amplifies by altering the microenvironment or stacking around DNA. In short: FRET drains AO's green output, while stacking and environmental changes push AO into red.

Variation with AO:RhB ratio

1: 0.5 → Limited RhB → partial energy transfer, mild red enhancement.

1: 1 and 1: 1.5 → Balanced donor–acceptor levels; FRET + AO metachromasy reinforce each other, giving the strongest ~650 nm emission.

1: 2 → Excess RhG quenches total fluorescence through *inner-filter effects* and self-absorption; common in concentrated rhodamines.

Quantify energy-transfer efficiency

To quantify energy-transfer efficiency, the following equation was used:

$$E = 1 - \frac{F_{DA}}{F_D}$$

Where F_D= AO–DNA fluorescence without RhG and F_{DA}=fluorescence with RhB. At 530nm.

The efficiency level can be used as a diagnostic indicator. For example, if the efficiency is high and stable (greater than 60%), it means that the genetic material has maintained its structural integrity, and the donor and acceptor remain at an optimal distance (within 10 nanometers). However, if there is a sharp decrease in efficiency (less than 40%), this indicates a collapse of the double-helix structure and a disordered binding state of acridine orange, reflecting the extent of molecular degradation or genetic damage.

CONCLUSION

The study presents a novel microchip-based optofluidic biosensor designed to detect early genetic damage related to cancer, using laser-induced fluorescence (LIF) and plasmonic enhancement on a gold-coated microfluidic platform. The chip integrates three inlets for controlled mixing of isolated DNA, acridine orange (AO), and rhodamine B (RhB) dyes at various ratios to optimize fluorescence resonance energy transfer (FRET), The goal is to enable early cancer detection through precise analysis of DNA fragmentation in lymphocytes, which often precedes malignant transformation. Traditional diagnostic techniques are often invasive, time-consuming, and physically stressful for patients. This system provides a fast, reagent-efficient, and highly sensitive alternative for detecting structural changes in DNA.

ACKNOWLEDGEMENT

This work supported by the ministry of higher education and scientific research (MOHESR) , the scientific research commission, and the university of Baghdad (UOB).

CONFLICT OF INTEREST

The authors declare that there is no conflict of interests regarding the publication of this manuscript.

REFERENCES

1. Song S-H, Lee TH, Her YS, Oh M, Shin DH, Heo Y, et al. Semen quality and sperm DNA fragmentation in cancer patients undergoing sperm cryopreservation. Investigative and Clinical Urology. 2023;64(5):489.
2. Alhmoud JF, Woolley JF, Al Moustafa A-E, Malki MI. DNA

Damage/Repair Management in Cancers. Cancers (Basel). 2020;12(4):1050.
3. Jackson SP, Bartek J. The DNA-damage response in human biology and disease. Nature. 2009;461(7267):1071-1078.
4. Wang M, Chen S, Ao D. Targeting DNA repair pathway in cancer: Mechanisms and clinical application. MedComm. 2021;2(4):654-691.
5. Tian H, Gao Z, Li H, Zhang B, Wang G, Zhang Q, et al. DNA damage response – A double-edged sword in cancer prevention and cancer therapy. Cancer Lett. 2015;358(1):8-16.
6. Nelson W, Soderlund C. Integrating sequence with FPC fingerprint maps. Nucleic Acids Res. 2009;37(5):e36-e36.
7. De Bont R. Endogenous DNA damage in humans: a review of quantitative data. Mutagenesis. 2004;19(3):169-185.
8. Pfeiffer P. Mechanisms of DNA double-strand break repair and their potential to induce chromosomal aberrations. Mutagenesis. 2000;15(4):289-302.
9. Darzynkiewicz Z, Bruno S, Del Bino G, Gorczyca W, Hotz MA, Lassota P, et al. Features of apoptotic cells measured by flow cytometry. Cytometry. 1992;13(8):795-808.
10. Bertho ÁL, Santiago MA, Coutinho SG. Flow cytometry in the study of cell death. Mem Inst Oswaldo Cruz. 2000;95(3):429-433.
11. Ribble D, Goldstein NB, Norris DA, Shellman YG. A simple technique for quantifying apoptosis in 96-well plates. BMC Biotechnol. 2005;5(1).
12. Kapuscinski J. DAPI: a DNA-Specific Fluorescent Probe. Biotechnic and Histochemistry. 1995;70(5):220-233.
13. Bruno S, Gorczyca W, Darzynkiewicz Z. Effect of ionic strength in immunocytochemical detection of the proliferation associated nuclear antigens p120, PCNA, and the protein reacting with Ki-67 antibody. Cytometry. 1992;13(5):496-501.
14. Millar AH, Liddell A, Leaver CJ. Isolation and Subfractionation of Mitochondria from Plants. Methods in Cell Biology: Elsevier; 2007. p. 65-90.
15. Delgir S, Bastami M, Ilkhani K, Safi A, Seif F, Alivand MR. The pathways related to glutamine metabolism, glutamine inhibitors and their implication for improving the efficiency of chemotherapy in triple-negative breast cancer. Mutation Research/Reviews in Mutation Research. 2021;787:108366.
16. Whitesides GM. The origins and the future of microfluidics. Nature. 2006;442(7101):368-373.
17. Duffy DC, McDonald JC, Schueller OJA, Whitesides GM. Rapid Prototyping of Microfluidic Systems in Poly(dimethylsiloxane). Anal Chem. 1998;70(23):4974-4984.
18. Yager P, Edwards T, Fu E, Helton K, Nelson K, Tam MR, et al. Microfluidic diagnostic technologies for global public health. Nature. 2006;442(7101):412-418.
19. Squires TM, Quake SR. Microfluidics: Fluid physics at the nanoliter scale. Rev Mod Phys. 2005;77(3):977-1026.
20. Iuay Hussein N, Al-Bawi Z. Microfluidic sensors platform technology to enhancement fluorescence. Bionatura. 2023;8(CSS 3):1-10.
21. Development of a Low-Cost Paper-Based Platform for Coffee Ring-Assisted SERS. American Chemical Society (ACS).
22. Principles of Fluorescence Spectroscopy. Springer US; 2006.
23. Nie S, Emory SR. Probing Single Molecules and Single Nanoparticles by Surface-Enhanced Raman Scattering. Science. 1997;275(5303):1102-1106.
24. Hindal SS, Al-Bawi ZF, Mahmood AI. Dual-substrate SERS sensor based on optical fiber for ultra-sensitive detection of organic pollutants. Optics Continuum. 2025;4(7):1505.
25. Khudhair WM, Al-Hayali SK, Al-Janabi A. No Core-Thin Core-No Core Optical Fiber Sensor Based MZI for in Time Detection of Bovine Serum Albumin. Sensing and Imaging. 2025;26(1).
26. Hussein Mahmood S, Kadhim Al-Hayali S, Al-Janabi A. Wide-range pH sensor based on a cascaded MZI up-down tapered hetero-core structure. Appl Opt. 2024;63(11):2906.
27. Mohammed DZ, Khaleel WA, Al-Janabi AH. Tunable Q-switched erbium doped fiber laser based on metal transition oxide saturable absorber and refractive index characteristic of multimode interference effects. Optics and Laser Technology. 2017;97:106-110.
28. Dina NA, Hanan JT. Enhancement of The Sensitivity of The Refractive Index Sensor Based on D-shaped Coreless Fiber. Iraqi Journal of Laser. 2024;23(2):85-96.
29. Al-dulimi S, Taher HJ. High-sensitivity drug biosensor based on taper and offset techniques for coreless optical fiber deposited with titanium dioxide nanoparticles. Optics Continuum. 2024;3(4):589.
30. Al-Awsaj NLH, Al-Bawi Z. A fluorescent biosensors for early detection of diabetes via lab on chips. AIP Conference Proceedings: AIP Publishing; 2024. p. 090002.
31. Lakowicz JR, Ray K, Chowdhury M, Szmacinski H, Fu Y, Zhang J, et al. Plasmon-controlled fluorescence: a new paradigm in fluorescence spectroscopy. The Analyst. 2008;133(10):1308.
32. Förster T. 10th Spiers Memorial Lecture. Transfer mechanisms of electronic excitation. Discuss Faraday Soc. 1959;27(0):7-17.
33. Clegg RM, Schneider PC. Fluorescence Lifetime-Resolved Imaging Microscopy: A General Description of Lifetime-Resolved Imaging Measurements. Fluorescence Microscopy and Fluorescent Probes: Springer US; 1996. p. 15-33.
34. Selvin PR. [13] Fluorescence resonance energy transfer. Methods in Enzymology: Elsevier; 1995. p. 300-334.
35. Al-Awsaj NlH, Al-Bawi Z, Mohammed SJ. Laser induced fluorescence technology for early detection of diabetes via optical fiber microfluidic sensor. Results in Optics. 2023;13:100557.
36. Hassanpour-Tamrin S, Sanati-Nezhad A, Sen A. A simple and low-cost approach for irreversible bonding of polymethylmethacrylate and polydimethylsiloxane at room temperature for high-pressure hybrid microfluidics. Sci Rep. 2021;11(1).
37. Prakash S, Kumar S. Fabrication of microchannels on transparent PMMA using CO_2 Laser (10.6 µm) for microfluidic applications: An experimental investigation. International Journal of Precision Engineering and Manufacturing. 2015;16(2):361-366.
38. Hubeatir KA, Al-Kafaji MM, Omran HJ. Deep Engraving Process Of PMMA Using CO_2 Laser Complemented By Taguchi Method. IOP Conference Series: Materials Science and Engineering. 2018;454:012068.
39. Moradi V, Akbari M, Wild P. A fluorescence-based pH sensor with microfluidic mixing and fiber optic detection for wide range pH measurements. Sensors and Actuators A: Physical. 2019;297:111507.
40. Cheng X, McCoy JH, Israelachvili JN, Cohen I. Imaging the Microscopic Structure of Shear Thinning and Thickening Colloidal Suspensions. Science. 2011;333(6047):1276-1279.
41. Jorgensen L, Wood GK, Rosenkrands I, Petersen C,

Christensen D. Protein adsorption and displacement at lipid layers determined by total internal reflection fluorescence (TIRF). J Liposome Res. 2009;19(2):99-104.
42. Zhao L, Cheng J. Analyzing the Molecular Kinetics of Water Spreading on Hydrophobic Surfaces via Molecular Dynamics Simulation. Sci Rep. 2017;7(1).
43. Aman ZM, Koh CA. Interfacial phenomena in gas hydrate systems. Chem Soc Rev. 2016;45(6):1678-1690.
44. Jiang Y, Xu Y, Wang R, Zhao B, Zhang X, Zhao H. Detection of Staphylococcus aureus using acridine orange-doped silica nanoparticles as a fluorescent label. RSC Advances. 2015;5(67):54338-54344.
45. Bag S, Hasan MI, Halder D, Ghosh A. Biosorption of organic dye Acridine orange from aqueous solution using dry biomass of Bacillus cereus M116. Arch Microbiol. 2021;203(7):3811-3823.
46. Rajeena U, Akbar M, Raveendran P, Ramakrishnan RM. Graphene reduction of P25 titania: Ti3+- doped titania/ graphene nanohybrids for enhanced photocatalytic hydrogen production. Int J Hydrogen Energy. 2020;45(16):9564-9574.
47. Sobhanardakani S, Jafari A, Zandipak R, Meidanchi A. Removal of heavy metal (Hg(II) and Cr(VI)) ions from aqueous solutions using Fe_2O_3@SiO_2 thin films as a novel adsorbent. Process Saf Environ Prot. 2018;120:348-357.
48. Han T, Wei Y, Jin X, Jiu H, Zhang L, Sun Y, et al. Hydrothermal self-assembly of α-Fe_2O_3 nanorings@graphene aerogel composites for enhanced Li storage performance. Journal of Materials Science. 2019;54(9):7119-7130.
49. Pivetta TP, Ribeiro PA, Raposo M. The Effect of UV-Vis Radiation on DNA Systems Containing the Photosensitizers Methylene Blue and Acridine Orange. Biophysica. 2024;4(1):22-33.
50. Liu C, Scott CN. Design strategies to rhodamine analogue fluorophores for near-infrared II biological imaging applications. Dyes and Pigments. 2021;196:109792.
51. Stockert JC, Blázquez-Castro A. Updating Ortho- and Metachromatic Acridine Orange Fluorescence in Cytochemical Chromosome Staining: A Proposal for Understanding Its Differential Fluorescence on Double- and Single-Stranded Nucleic Acids Substrates Based on Intercalation. Chemosensors. 2023;11(10):540.